

Recyclable Biomimetic Sunflower Pollen-based Photocatalyst for Enhanced Degradation of Pharmaceuticals

Miquel Ortiz, Elvira Gómez, and Albert Serrà*

Recent trends in addressing the impending water crisis focus on the development of innovative water treatment methods. This work utilizes pollen as a core template to synthesize highly efficient onion-like photocatalysts for pollutant mineralization. The study showcases a novel electrochemical synthesis method that maintains the structural integrity of pollen, resulting in increased surface area and enhanced photocatalytic activity. After 90-min of visible light irradiation, over 99% mineralization is achieved. These hybrid photocatalysts demonstrate exceptional stability and efficacy in degrading pollutants. The used photocatalysts can be recycled into biopellets with an ash content of less than 7% (weight), moisture content of less than 8% (weight), and a calorific value of $\approx 22.1 \pm 0.3 \text{ MJ kg}^{-1}$. Additionally, the resulting ashes serve as effective peroxymonosulphate activators for pollutant mineralization. This process offers sustainable waste management while minimizing waste production, providing a practical solution for water purification. The efficacy of this approach in pollutant removal is underscored by mineralization rates exceeding 99%.

energy conservation, mild reaction conditions, and minimal secondary pollution. Nevertheless, the current generation of photocatalysts, particularly those that employ visible light and solar energy, face significant challenges in terms of scalability, high production costs, and operational issues related to photo-reactors. Furthermore, micro- and nano-scale catalysts are challenging to separate and reuse.^[5,11–14]

Researchers are currently engaged in the development of novel photocatalytic materials that are characterized by enhanced stability, high activity, and the capacity for large-scale production from abundant sources.^[15–18] Copper oxide semiconductors, with their lower band gap, represent a promising alternative to traditional photocatalysts. These materials are capable of generating reactive oxygen species (ROS) across the visible and even infrared spectra.

Nevertheless, $\text{Cu}_2\text{O}/\text{CuO}$ semiconductors are prone to rapid electron-hole recombination and low photostability, which results in diminished efficiency and increased susceptibility to photocorrosion.^[19–22]

It has been proposed that measures be taken to improve the stability of the external CuO layer. This is based on the findings that photocorrosion is mainly the result of the accumulation of photo-induced electrons in the CuO shell, which then leads to the self-reduction of CuO to Cu_2O . The principal strategies to overcome photocorrosion involve the formation of heterojunction materials, which accelerate the exportation of photo-induced electrons and holes. Notwithstanding the fact that metallic sulfides are prone to high levels of photocorrosion when subjected to irradiation, which can result in the leaching of metals and the production of sulfur (in the absence of oxygen) or sulfate (in the presence of oxygen), metallic sulfide-based heterojunctions have demonstrated efficacy in impeding the progression of photocorrosion. In order to address these limitations, researchers have investigated CuO-CuS heterojunctions.^[22–24] These heterojunctions facilitate the transfer of charge carriers between semiconductors, thereby mitigating rapid electron-hole pair recombination. Furthermore, the photostability of $\text{CuO-Cu}_2\text{O}$ semiconductors is enhanced by the incorporation of protective shells, such as CuS .^[20–22,24] The CuO-CuS heterojunction has demonstrated enhanced performance in comparison to the individual CuO and CuS components.^[19] Notwithstanding these advances, further improvements are required for practical applications.

1. Introduction

It is estimated that over one billion people in arid regions will experience severe clean water shortages this decade as a result of contamination by organic compounds from industrial, agricultural, and urban activities.^[1,2] These pollutants, including pesticides and pharmaceuticals, present a significant environmental and public health risk due to their toxicity.^[3–5] Conventional water treatment methods often prove ineffective in the removal of these pollutants.^[3,6–10]

Photocatalysis has emerged as a promising method for water treatment, offering several advantages including efficiency,

M. Ortiz, E. Gómez, A. Serrà
Grup d'Electrodeposició de Capes Primes i Nanoestructures (GE-CPN)
Departament de Ciència de Materials i Química Física
Universitat de Barcelona
Institute of Nanoscience and Nanotechnology (IN²UB)
Universitat de Barcelona
Martí i Franquès, 1, Barcelona, Catalonia E-08028, Spain
E-mail: a.serra@ub.edu

 The ORCID identification number(s) for the author(s) of this article can be found under <https://doi.org/10.1002/smll.202405204>

© 2024 The Author(s). Small published by Wiley-VCH GmbH. This is an open access article under the terms of the [Creative Commons Attribution License](https://creativecommons.org/licenses/by/4.0/), which permits use, distribution and reproduction in any medium, provided the original work is properly cited.

DOI: 10.1002/smll.202405204

Biomimetic photocatalysts, which are inspired by natural processes, have the capacity to enhance photocatalytic activity by improving light capture and absorption. These catalysts emulate natural designs, such as the photosynthetic structures of leaves or the light-absorbing properties of certain insects, to create materials that efficiently harness light energy. The generation of charge carriers by irradiation results in the production of reactive species that are capable of fully oxidizing organic pollutants.^[25–28]

It is of paramount importance to achieve efficient photon harvesting at the semiconductor surface in order to attain a high quantum yield. Biomimicry optimizes light harvesting by enhancing surface light coupling, trapping light in weakly absorbed wavelengths, and minimizing optical losses. Natural designs offer non-reflective surfaces with sub-wavelength structures or hierarchical micro- and nano-scale architectures that reduce light losses, thereby enhancing the efficiency of light capture.^[6,25–28]

Biotemplates derived from algae and other microorganisms are employed in the synthesis of photocatalysts through straightforward, environmentally benign, and scalable methodologies.^[29–31] The non-reflective coatings inspired by the optics of moth eyes and butterfly wings have the potential to facilitate efficient light harvesting and, consequently, the decontamination of water. The blueprints for intelligent photocatalysts with improved light absorption and pollutant degradation can be found in plants and trees.^[6,26]

This biomimetic approach is aligned with the goals of circular economy and sustainability, employing abundant and nontoxic materials for the scalable synthesis of micro- and nano-architectures.^[12,25,32] Pollen, with its uniform carbon skeleton, substantial pore volumes, high surface areas, and unique 3D network structure, is a promising material for further investigation. The utilization of diverse pollen types, including those derived from rape, dandelion, and lotus, as additives in metal oxide synthesis, presents a cost-effective and environmentally friendly alternative to conventional methods.^[12,17,33–39]

In this study, a 3D onion-like pollen-Cu@Cu₂O@CuO@CuS photocatalyst is successfully synthesized using a sequential, cost-effective, and scalable electrochemical production strategy. The distinctive architecture of the sunlight pollen contributes to its porous structure and high surface area, providing active sites for reactions and facilitating the separation of photogenerated electrons and holes, thus enhancing light harvesting and ROS generation. The pollen-Cu@Cu₂O@CuO@CuS photocatalyst exhibits a high removal yield (84.4% ± 0.8%) and substantial mineralization (99.5% ± 0.3%) under simulated solar conditions, indicating its broad spectral absorption range and practical applicability. Additionally, the material demonstrates notable stability against photocorrosion, particularly in slightly alkaline conditions, due to the protective CuS external layer.

Moreover, the principles of a green and circular economy are integrated through the utilization of an organic matrix in the fabrication of biopellets. The biopellets satisfy the ISO 17225–6:2014 standards for non-wood pellets, exhibiting an ash content of less than 7%, a moisture content of less than 10%, and a calorific value of ≈22.1 MJ kg⁻¹. The ashes resulting from the combustion of biopellet act as catalysts, facilitating the generation of sulfate radicals from peroxymonosulfate. This process enables the mineralization of 60 ppm drug solutions within a relatively short time frame. This research underscores the potential of nat-

ural pollen-based photocatalysts for effective pollutant removal and water purification. Additionally, it contributes to the advancement of waste-to-energy conversion and sustainable material innovation.

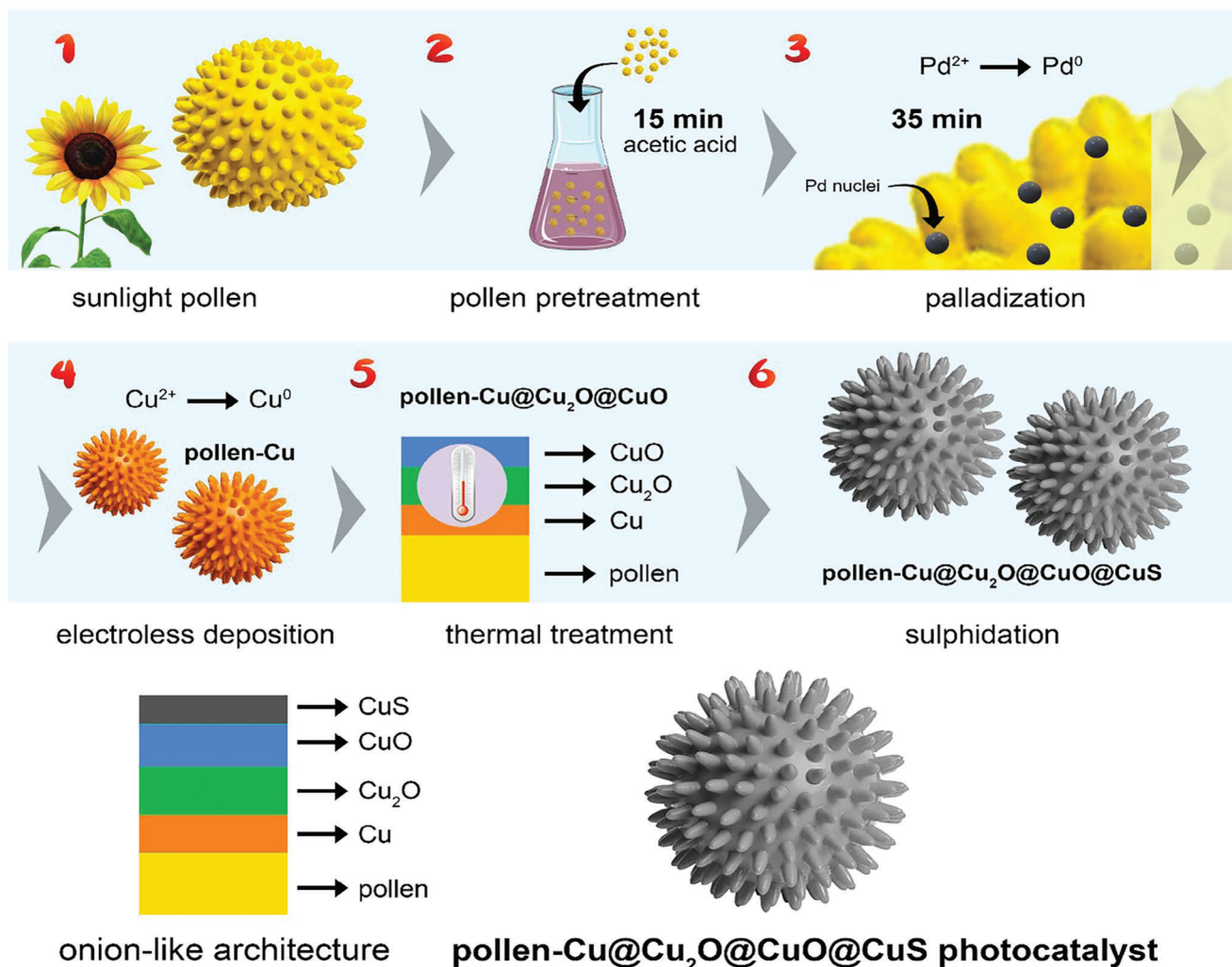
2. Results and Discussion

2.1. Electrosynthesis and Characterization of Pollen-Cu@Cu₂O@CuO@CuS Photocatalyst

Scheme 1 depicts the sequential, scalable synthesis of the pollen-Cu@Cu₂O@CuO@CuS photocatalyst. The process comprises a series of steps, including pollen pretreatment, palladization, electroless deposition, thermal treatment, and chemical sulfidation. Sunflower pollen was selected due to its echinate and tricolporate structure (**Figure 1a**), which renders it a promising candidate for enhancing light harvesting and pollutant adsorption. Pollen grains are employed as cost-effective and sustainable templates that are readily available in large quantities. The structure is multilayered and coated with an external layer, known as pollenkitt. The layer in question may also contain environmental contaminants and allergens, which can fill nanopores on the surface.

Prior to electrosynthesis, the pollen biomass was treated with glacial acetic acid to disrupt the cell walls of the pollenkitt, thereby exposing the underlying microporous structures. As illustrated in **Figure 1b**, the structural integrity and size uniformity of the pollen grains were maintained following the destruction of the pollenkitt, indicating that no denaturation occurred. Subsequently, the pollen was subjected to a stannous palladization bath under acidic conditions to facilitate the formation of Pd nuclei on the biomaterial's surface. Following the cleaning of palladized pollen, a color shift from intense yellow to brown was observed (**Figure S1a,b**, Supporting Information), which may be indicative of the formation of Pd nuclei on the biomaterial's surface. Energy-dispersive X-ray spectroscopy (EDS) analysis confirmed the presence of Pd nuclei on the pollen surface. Subsequently, the palladization was followed by the electrochemical deposition of copper, a process that involves electroless plating.

Electroless plating is a method that involves the deposition of a metal film onto a substrate through a redox reaction. In this study, copper (II) sulfate and formaldehyde were used in an alkaline reaction bath. This resulted in the reduction and deposition of copper, forming a continuous, homogeneous nanometric layer onto the pollen grains (**Figure 1c**), while maintaining the complex spikes architecture. Subsequently, the color of the pollen changed to an intense brown hue (**Figure S1c**, Supporting Information), which is characteristic of copper materials. Following the electroless treatment, the pollen was subjected to an oven at 200 °C for 8 h, resulting in the formation of a hybrid external layer of Cu₂O and CuO. This resulted in the formation of a heterostructured pollen-Cu@Cu₂O@CuO. Subsequently, the biomaterial exhibited a pale gray coloration following the oxidation treatment (**Figure S1d**, Supporting Information). Finally, the material was subjected to a sulfidation treatment, whereby it was immersed in a thioacetamide solution for a period of 4 h. This resulted in a coal-like black color (**Figure S1e**, Supporting Information). The resulting photocatalyst was composed of a pollen core encased in Cu@Cu₂O@CuO@CuS shells (**Figure 1e**). The presence of copper on the photocatalyst's surface, resulting from



Scheme 1. Schematic representation of the multi-step sequential synthesis process of pollen-Cu@Cu₂O@CuO@CuS photocatalysts.

the electroless plating process, was confirmed through the use of field-emission scanning electron microscopy (FE-SEM) images and elemental analysis. The appearance of sulfur was observed post-treatment with thioacetamide, which suggests the successful formation of each layer. Figure 1 presents a comprehensive elemental analysis of carbon, oxygen, sulfur, tin, palladium, and copper, accompanied by additional FE-SEM images of the raw pollen and synthesis intermediates.

An additional pivotal factor to be taken into account is the thermal stability of pollen and hybrid photocatalysts. To assess this, a thermogravimetric analysis (TGA) was performed over a temperature range of 30 to 800 °C (Figure 2a). It is important to note that the temperatures typically employed in water treatment processes range from 20 to 50 °C. Within this range, the mass variation of both pollen and pollen-Cu@Cu₂O@CuO@CuS photocatalysts was found to be minimal, with a maximum variation of less than 0.03%. While this stability at lower temperatures may appear inconsequential for applications involving water immersion, it was imperative to demonstrate that the pollen retained its characteristics throughout the thermal treatment necessary for synthesis. During the synthesis process, the pollen-Cu hy-

brid was subjected to an oven maintained at 200 °C for a period of 8 h. In both cases, whether uncoated or coated pollen, the mass loss during this treatment was less than 0.3%. Upon examination of the stability of the materials at elevated temperatures, a small disparity in thermal stability was observed between the coated and uncoated pollen. In the presence of air and up to a temperature of 800 °C, the uncoated pollen exhibited a mass loss of 1.4%, whereas the pollen-Cu@Cu₂O@CuO@CuS photocatalysts demonstrated a reduced mass loss of 0.7%. This indicated that the coating not only enhanced the photocatalytic properties of the material but also improved its thermal stability.

Figure 2b shows the X-ray diffraction (XRD) pattern of the hybrid photocatalysts. The diffraction pattern was complex and showed numerous peaks. Two distinct peaks, highlighted with black circles, appeared at 2θ values of 25.8° and 33.7°, corresponding to the pollen prior to the coating process. The other peaks could not be assigned to a single phase but were aligned with cubic Cu (JCPDS 00-004-0836), CuO (JCPDS 01-080-0076), Cu₂O (JCPDS 00-034-1354), and CuS (JCPDS 00-006-0464). Although it was not possible to assign the peaks to a single crystalline phase due to the heterogeneity of the system and the

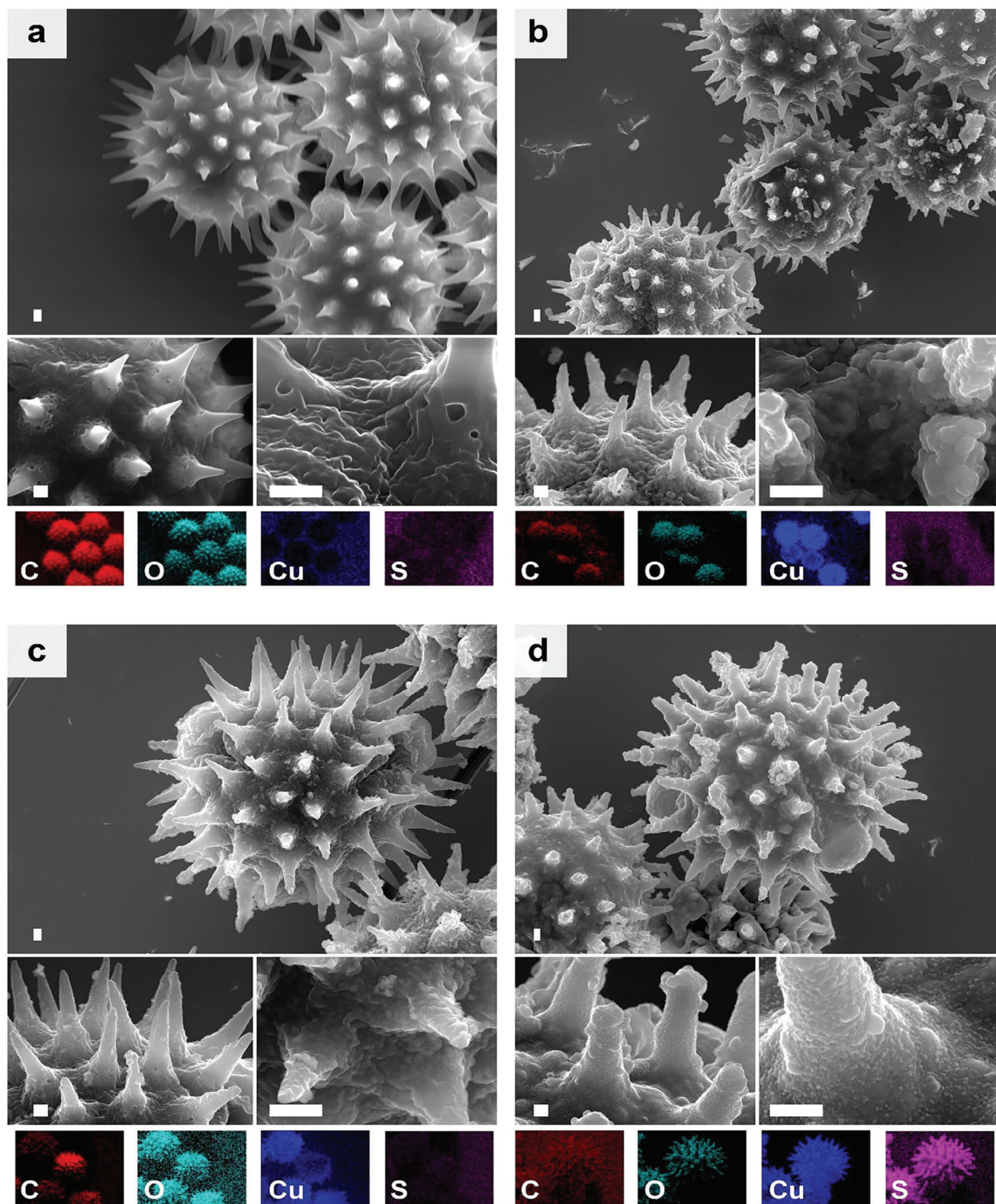


Figure 1. FE-SEM micrographs and elemental mapping analysis of a) pollen; b) pollen-Cu, c) pollen-Cu@Cu₂O@CuO, and d) pollen-Cu@Cu₂O@CuO@CuS powders. Scale bar: 1 μ m.

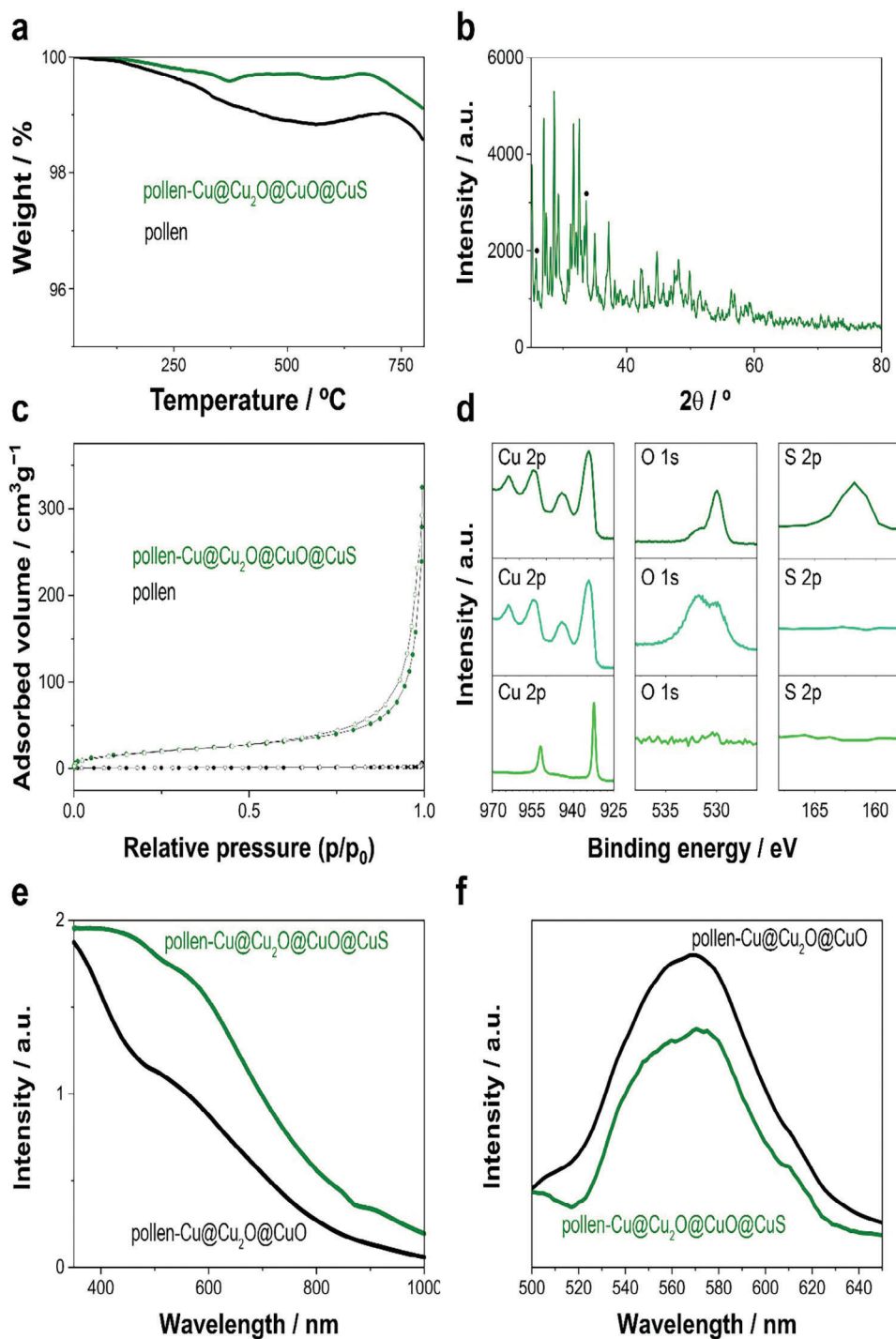


Figure 2. a) Thermogravimetric analysis of pollen and pollen-Cu@Cu₂O@CuO@CuS powders. b) XRD patterns of pollen-Cu@Cu₂O@CuO@CuS powders. The black circles indicate the peaks corresponding to the pollen substrate before and after thermal treatment. c) Nitrogen adsorption-desorption isotherms of pollen, and pollen-Cu@Cu₂O@CuO@CuS powders. d) XPS spectra of the pollen-Cu@Cu₂O@CuO@CuS hybrids. The upper section of the graph represents the external layer, the middle section represents the intermediate layer, and the lower section represents the innermost layer of the onion-type structure. e) UV-Vis diffuse reflectance and f) photoluminescence spectra of pollen-Cu@Cu₂O@CuO@CuS hybrids.

different mixtures likely present in each pollen grain, XRD analysis confirmed that the multi-step process successfully yielded pollen-Cu@Cu₂O@CuO@CuS hybrid photocatalysts.

The surface area of the coated pollen, as determined by Brunauer-Emmett-Teller (BET) analysis, was found to be 70.2 m² g⁻¹ (Figure 2c), a significant increase compared to the uncovered pollen (1.71 m² g⁻¹). This notable difference could be attributed to the apparent roughness observed on the surface of the photocatalyst, as shown in more magnified FE-SEM images shown in Figure 1. It is noteworthy that the spike structure was maintained, coupled with a significant increase in surface area (multiplied by ≈41 when considering the mass of the whole unit). It is important to note that this value becomes even more significant when considering only the mass of the external Cu@Cu₂O@CuO@CuS multilayers. The increased surface area was expected to enhance light harvesting, pollutant adsorption, and reactive oxygen species formation, thereby improving the performance of the photocatalyst.

X-ray photoelectron spectroscopy (XPS) analysis was used to investigate the chemical nature of the photocatalyst surface after undergoing Cu electroless deposition, thermal treatment, and sulfidation processes (Figure 2d). To avoid sample charging effects, the binding energies obtained from the XPS analysis were calibrated by referencing the C 1s peak to 284.60 eV. The sputtering time for the depth profile was maintained at 900 s with 30-s intervals throughout the analysis. Figure 2d shows the XPS spectra at different depths. The top part represents the outer layer, while the bottom part represents the innermost layer.

In the innermost layer, 2 prominent peaks were observed in the Cu 2p spectra at 932.6 and 952.8 eV, corresponding to Cu(0) and attributed to Cu 2p_{3/2} and Cu 2p_{1/2}, respectively, confirming the successful deposition of Cu(0). No presence of S was detected at this level, while traces of oxygen were identified. Moving to the intermediate layer, the Cu 2p spectra exhibited 2 primary asymmetric peaks centered at 954.5 and 934.3 eV, representing Cu 2p_{1/2} and Cu 2p_{3/2}, respectively. Two additional peaks centered at 964.2 and 944.3 eV were observed, due to the satellite peaks of Cu₂O and CuO, respectively. Deconvolution of the main peaks revealed 4 peaks at 953.4 and 933.6 eV, corresponding to Cu 2p_{1/2} and Cu 2p_{3/2} of Cu⁺, confirming the presence of Cu₂O, and 955.7 and 935.2 eV, corresponding to Cu 2p_{1/2} and Cu 2p_{3/2} of Cu⁺, confirming the formation of CuO, respectively.^[40–42] In addition, a distinct asymmetric peak was observed in the O 1s region, which was deconvoluted into 2 peaks centered at 531.6 and 529.8 eV. The 529.8 eV peak was attributed to lattice oxygen from both Cu₂O and CuO phases, while the 531.6 eV peak was related to surface hydroxyl groups.^[42] No signal was detected for S 2p, either on the surface or in subsequent layers.

Upon analyzing the external layer, it was found that the Cu 2p spectra resembled those obtained after thermal treatment. Additionally, the O 1s spectra showed an asymmetric peak, which was composed of contributions from both lattice oxygen and surface hydroxyl groups. The S 2p XPS spectra of the external layer revealed the formation of a CuS layer, with peaks centered at 162.7 and 161.4 eV for S 2p_{1/2} and S 2p_{3/2}, respectively. Therefore, the XPS analysis confirmed the formation of an onion-like pollen-Cu@Cu₂O@CuO@CuS architecture.

Figure 2e shows the UV–Vis diffuse reflectance spectra of pollen-Cu@Cu₂O@CuO@CuS hybrids, which exhibit a broad

absorption range in the visible light and near-infrared (NIR) regions. In comparison to pollen-Cu@Cu₂O@CuO heterostructures, the pollen-Cu@Cu₂O@CuO@CuS hybrids exhibit a notable redshift, thereby enhancing their photocatalytic activity under visible-light irradiation. The heterostructured architecture enables bandgap engineering, thereby facilitating more efficient charge transfer between the components. This can result in the formation of intermediate energy states within the band gap, thereby enabling the absorption of longer wavelengths and the observed red shift in the absorption spectrum. Furthermore, the heterostructured architecture facilitates enhanced light harvesting due to the synergistic effects between the materials.

Figure 2f presents the photoluminescence spectra of the hybrids, which exhibit a broad emission peak at $\lambda = 571$ nm when excited at 400 nm. The photoluminescence emission intensity of these hybrids was markedly lower than that of pollen-Cu@Cu₂O@CuO heterostructures, indicating the effective suppression of electron-hole recombination due to the enhanced electron transfer within the onion-like architecture. The diminished photoluminescence intensity indicates enhanced photocatalytic efficiency, as it is indicative of reduced charge carrier recombination. The incorporation of an external CuS layer has been demonstrated to enhance the separation and migration of charge carriers. These characteristics render the pollen-Cu@Cu₂O@CuO@CuS biohybrids highly promising for visible-light-driven photocatalytic water decontamination.

2.2. Photocatalytic Performance for Degrading and Mineralizing Pharmaceuticals

The objective of the study was to ascertain the stability of tetracycline (TC) at pH 6.0 and 8.5 over a 30-day period. Figure S2 (Supporting Information) illustrates the UV–Vis spectra, which indicate a slight decline in absorbance in slightly acidic conditions, representing a mere 7% degradation. These findings indicate that TC is relatively stable at pH 6.0. However, at pH 8.0, the degradation increased to 26% by the 30th day. Nevertheless, the decline in concentration was still regarded as minimal, particularly when considering the extensive study period. It is noteworthy that TC did not undergo mineralization, as the variation in total organic carbon (TOC) was less than 1%, irrespective of pH.

As with non-photolytic degradation, photolysis proved more effective at pH 8.0. Following 180 min of irradiation, the UV–Vis spectra (Figure S3, Supporting Information) indicated less than 3% and 15% degradation for slightly acidic and basic conditions, respectively. These findings indicate that photolysis is an ineffective treatment for TC-contaminated waters. Mineralization was essentially absent, with less than 1% TOC decay observed in the absence of light, irrespective of pH.

To enhance the degradation and mineralization performance of TC, the adsorption-desorption of the antibiotic onto the photocatalyst surface was studied. UV–Vis tests were conducted during the 120-min adsorption-desorption study. As illustrated in Figure S4 (Supporting Information), the absorbance exhibited a decline at both pH levels under examination. The maximum adsorption, which reached equilibrium, occurred at 80 min for both pH values. The adsorption process was found to follow a pseudo-first-order kinetic model. The efficiency of the adsorption process is

dependent upon the charge of both the contaminant and the surface of the photocatalyst. The isoelectric point of CuS is typically reported to occur between pH 3 and 5, where the surface exhibits a net zero charge. At pH values exceeding 5, the CuS surface acquires a negative charge. At pH 6, TC exists in its zwitterionic form, whereas at pH 8, it is predominantly negatively charged. Although one might anticipate greater adsorption in the vicinity of pH 6, given the electrostatic interactions, the experimental results showed that adsorption was actually more pronounced at pH 8 compared to pH 6.

The photocatalytic activity of pollen-Cu@Cu₂O@CuO@CuS hybrids was evaluated for the degradation and mineralization of TC under visible light irradiation. The recorded UV-Vis spectra (Figure 3a) showed a notable decline in absorbance over the course of 90 min. The findings revealed that degradation occurred more rapidly in slightly alkaline conditions, with minimal absorbance observed after 60 min. In contrast, some TC remained in slightly acidic conditions at the end of the study. The complete degradation of TC in mildly acidic conditions required a period of over 120 min. The observed favored degradation in slightly alkaline conditions can be attributed to the enhanced stability of TC in neutral and acidic conditions and to the increased adsorption on the photocatalyst surface at basic pH, which facilitates the process. The degradation kinetics were analyzed using the Langmuir-Hinshelwood model, with a pseudo-first-order kinetic model (Figure S5, Supporting Information) fitted to the data. Despite the difficulties in comparing the catalytic activities of different photocatalysts, these materials demonstrate comparable photocatalytic performance to that of current state-of-the-art systems.^[43–47] The TOC analysis (Figure 3b) demonstrated that the mineralization of organic matter was more pronounced under slightly basic conditions at both 60 and 90 min after the start of photocatalysis, confirming the mineralization of TC. Following a 60-min photocatalytic process, the total mineralization reached 64.9% ± 0.7% and 96.0% ± 0.5% in slightly acidic and slightly basic conditions, respectively. By 90 min, these values had increased to 79.4% ± 0.8% and 99.5% ± 0.3%, respectively. The near-identical correlation between the degradation and mineralization percentages indicated that the photocatalyst rapidly degraded TC intermediates until complete mineralization was attained.

The mechanism of TC degradation was investigated using specific quenchers. The following quenchers were employed: IPA (hydroxyl radical quencher), BQ (superoxide radical quencher), and TEA (valence band hole quencher). To circumvent the limitations of UV-Vis spectrophotometry, high-performance liquid chromatography-mass spectrometry (HPLC-MS) was employed to monitor the degradation process. Figure 3c illustrates a notable decline in photocatalytic performance when TEA was present, with less pronounced reductions observed with IPA and BQ. This trend persisted across both pH conditions.

The degradation rate of TC was reduced by more than 2.6 times at pH 6 and over 7.6 times at pH 8.5 in the presence of TEA, compared to the absence of scavengers. With IPA, the reduction was 1.6 times at pH 6 and ≈2.0 times at pH 8.5, again compared to the absence of scavengers. The presence of alkaline solutions, with hydroxide ions, could facilitate the interaction of these ions with photogenerated holes on the photocatalyst surface, resulting in the production of highly reactive and non-selective hydroxyl

radicals.^[48] These radicals are highly effective in degrading a wide range of organic pollutants, including TC, and their formation also reduces electron-hole recombination.

The photocatalytic degradation of TC by pollen-Cu@Cu₂O@CuO@CuS was primarily driven by photogenerated holes, followed by hydroxyl radicals, with superoxide radicals contributing the least. The degradation efficiency was enhanced in slightly alkaline conditions (pH 8.5) due to the increased generation of hydroxyl radicals from the presence of hydroxide ions. While holes could directly oxidize TC, their primary function was to facilitate the production of hydroxyl radicals. At slightly acidic pH, the degradation rate reduction was ≈2.7 times that observed at neutral pH, while at alkaline pH, it was reduced up to 7.6 times. This suggested that the primary function of photogenerated holes was to form hydroxyl radicals, rather than directly oxidizing TC. The substantial decline in degradation with TEA underscored the pivotal role of photogenerated holes. The effective utilization of these holes and reduced electron-hole recombination contributed to enhanced photocatalytic performance in alkaline solutions, aligning with the experimental findings that highlighted the predominance of photogenerated holes in this process.

The efficacy of AOPs is typically contingent upon the intricate, multi-component nature of the wastewater being treated. The presence of inorganic anions in the aqueous matrix can either impede or facilitate the photocatalytic process. The effects of chloride, nitrate, and phosphate anions, which are commonly found in wastewater, on the photocatalytic degradation and mineralization of TC have been studied individually. However, when attempting to track the degradation of TC using UV-Vis spectroscopy, overlapping peaks were observed, likely due to the formation of intermediates. Therefore, the effect of these anions could only be determined by HPLC-MS and TOC analysis.

The results demonstrated notable discrepancies in the extent of degradation and mineralization contingent on the anion and pH (Figure 3d). The presence of chloride ions was observed to exert a slight inhibitory effect under alkaline conditions. This can be attributed to the formation of less reactive chloride radicals, which act as scavengers for reactive species like hydroxyl radicals and holes.^[49,50] Surprisingly, an increase in mineralization was observed in acidic conditions, increasing with NaCl concentration, which may indicate that chloride has a promoter role in these conditions. This promoting effect may be attributed to chloride's interaction with other reactive species or its contribution to the formation of active intermediates that enhance TC breakdown. Furthermore, chloride may influence the speciation of TC or other components present in the reaction mixture, potentially rendering TC more susceptible to mineralization.^[49,50]

The presence of nitrates was observed to exert an inhibitory effect at both pH levels, with a more pronounced impact observed in acidic conditions. At a concentration of 100 mM, the degradation and mineralization processes exhibited a reduction of 6%–11%. In contrast, the reduction was less than 2% in alkaline conditions. They facilitate the formation of reactive nitrogen species and hydroxyl radicals, which enhance the breakdown of organic matter. Nevertheless, they can also function as electron and hole scavengers generated by photochemical processes.^[51,52] The findings suggest that, in this particular case, nitrate exerts a slight inhibitory effect on the mineralization performance of TC.

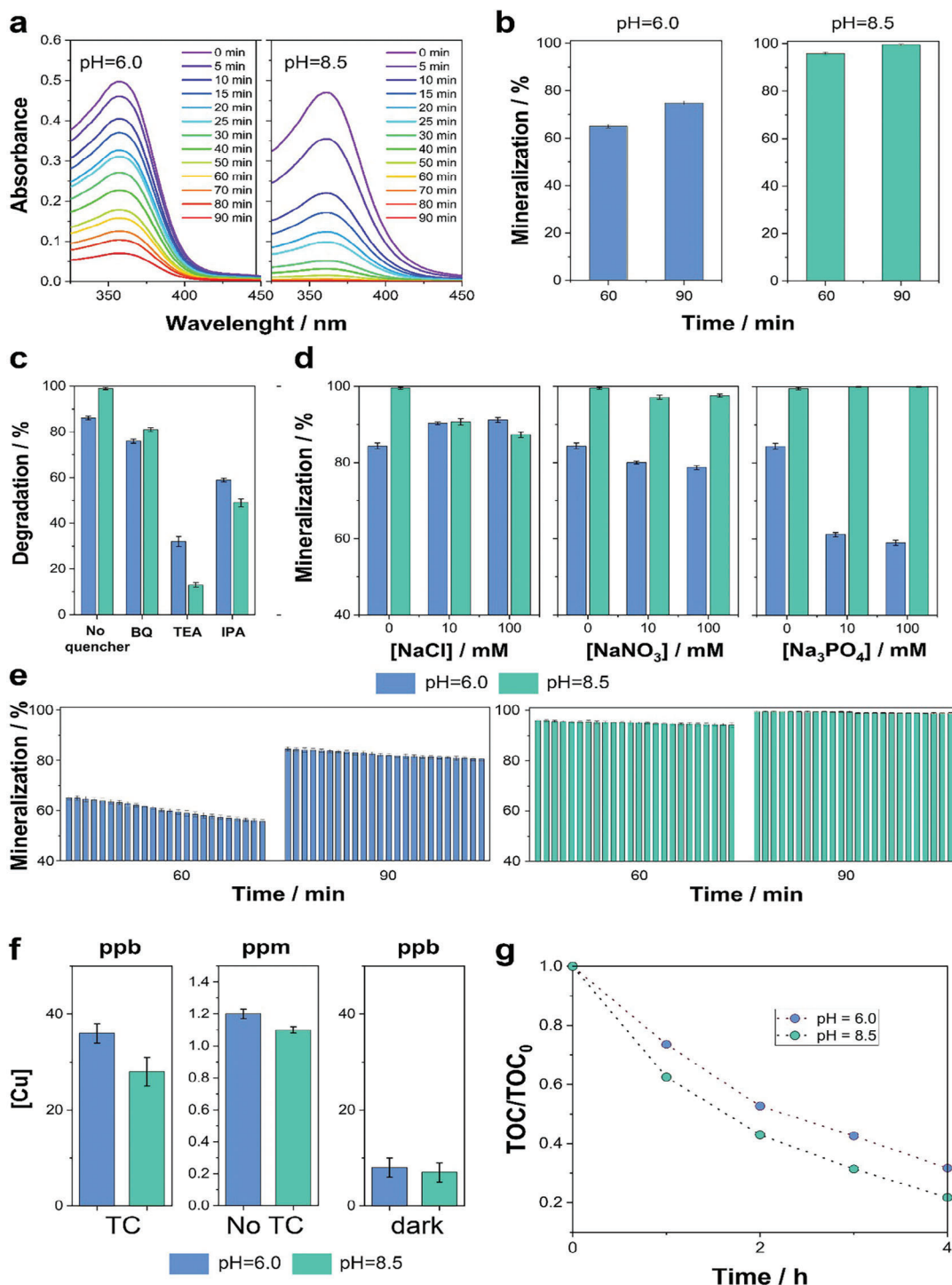


Figure 3. a) Time-dependent UV–Vis spectra (325–450 nm) of TC over 90 min under visible-light irradiation at pH 6.0 (left) and 8.5 (right). b) Mineralization of a 20 ppm TC solution after 60 and 90 min of visible light irradiation at pH 6.0 (left) and 8.5 (right). c) Degradation of a 20 ppm TC solution after 90 min of visible light irradiation at pH 6.0 and pH 8.5 in the presence of 1 mM concentration of quenchers. d) Mineralization performance of a 20 ppm TC solution after 90 min of visible light irradiation at pH 6.0 and pH 8.5 in the presence of sodium chloride, sodium nitrite, and sodium phosphate. e) Total mineralization of TC at 60 and 90 min for 24 consecutive cycles of visible light irradiation at pH 6.0 (left) and 8.5 (right). f) Released copper during 24 consecutive reusability cycles for degrading 20 ppm of TC (left), 36 h in the absence of contaminants (middle), and 36 h in the absence of contaminants and dark conditions (right) at pH 6.0 and pH 8.5. Experimental conditions: 20 ppm of tetracycline, photocatalyst dose = 0.4 mg mL⁻¹, and T = 20 °C. g) TOC decay of a multipollutant solution containing 20 ppm of lansoprazole, 20 ppm of levofloxacin, and 20 ppm of tetracycline during 4 h under visible light irradiation at pH 6.0 and pH 8.5, photocatalyst dose = 0.4 mg mL⁻¹. The error bars represent the standard deviations from 3 replicate experiments.

In regard to phosphates, it is noteworthy that 2 distinct species are predominant at each pH. At pH 6.0, dihydrogen phosphate (H_2PO_4^-) predominates, while at pH 8.5, hydrogen phosphate (HPO_4^{2-}) is majoritarian. This provides a partial explanation for the markedly disparate effects observed at each pH level. In acidic conditions, mineralization decreased from $84.4\% \pm 0.8\%$ to $59.0\% \pm 0.7\%$, representing a significant reduction. However, in alkaline conditions, mineralization was favored by the presence of phosphate, approaching total TC mineralization. In fact, mineralization already exceeded 99% after 60 min of photocatalysis at both 10 and 100 mM concentrations. Phosphate has been reported to have an inhibitory effect due to rapid adsorption on the surface of some photocatalysts, which may explain the effects observed at acidic pH. However, recent research has proposed that phosphate may also act as a promoter by forming a more reactive radical in the presence of photogenerated holes.^[53–55] As the dominance of holes in the degradation of TC was confirmed in this process, it lends support to this theory. Nevertheless, this theory is unable to account for the significant discrepancies observed between our acidic and basic conditions. Additionally, the formation of this radical species should be more favored in acidic conditions, since H_2PO_4^- is the predominant species.

The literature states that the efficiency of CuO, Cu_2O , and CuS photocatalysts is often limited by their low resistance to photocorrosion, leading to a decline in performance after just a few cycles. Upon photoexcitation, CuO undergoes self-reduction due to photogenerated electrons, which represents a primary factor in its photocorrosion. Two mechanisms are responsible for the photocorrosion of photoexcited Cu_2O : self-photoreduction to metallic Cu by photogenerated electrons and self-photooxidation to CuO by photogenerated holes. Similarly, photoexcited CuS undergoes photobleaching of copper ions. In the absence of oxygen, copper sulfide can undergo photocorrosion in aqueous solutions, resulting in the production of sulfur. In contrast, in the presence of oxygen, the photocorrosion process involves the oxidation of sulfide to sulfate.^[56–58] Nevertheless, the formation of heterostructured Cu-based materials can markedly alleviate the photocorrosion process by expediting the separation and transport of photo-induced electrons and holes. To address this issue, Cu@CuO@ Cu_2O heterojunctions have been demonstrated to effectively increase photocorrosion resistance.^[19,20,40] The objective of this study was to evaluate the impact of a CuO@ Cu_2O @CuS heterojunction on the reusability and photocorrosion resistance capacity of the photocatalyst. The study examined the photocatalytic mineralization of TC over 24 consecutive cycles at pH values of 6.0 and 8.5. TOC measurements were taken at 60 and 90 min, as illustrated in Figure 3e. The results indicate that mineralization was more effective in basic conditions, with a negligible decline of $\approx 0.8\%$ after 24 cycles, which is within the margin of error associated with TOC measurements. Nevertheless, a somewhat greater decline in mineralization ($\approx 1.9\%$) was noted after 60 min of photocatalysis. These findings illustrate that the material exhibits robust resistance to photocorrosion in basic conditions. In contrast, the efficiency of the process was found to be significantly reduced in pH 6, particularly during the 60-min interval, where a 14% decrease in mineralization was observed after 24 cycles. Nevertheless, after 90 min, the decline in performance was less than 5%. The findings indicate that the resistance to photo-

corrosion was less robust at pH 6.0 than at pH 8.5. After 60 min, the photocatalysts displayed indications of attrition, particularly in acidic conditions. Nevertheless, the Cu@CuO@ Cu_2O @CuS heterojunctions exhibited the capacity to enhance the reusability of the Cu-based photocatalyst in water treatment. Moreover, the integrity of the hybrids was verified through FE-SEM observation (Figure S6, Supporting Information).

The direct photocorrosion of pollen-Cu@ Cu_2O @CuO and pollen-Cu@ Cu_2O @CuO@CuS was investigated to ascertain whether the sulfidation process resulted in enhanced photochemical stability. For these experiments, the concentration of Cu ions in the 24 solutions treated with both photocatalysts was found to be below 480 ppb for pollen-Cu@ Cu_2O @CuO and 40 ppb for pollen-Cu@ Cu_2O @CuO (Figure 3f), irrespective of the pH of the reaction medium. It is noteworthy to note that the concentration of Cu ions in the solution increased to 3.1 ppm and 1.2 ppm for pollen-Cu@ Cu_2O @CuO and pollen-Cu@ Cu_2O @CuO@CuS, respectively, when the photocatalyst was subjected to the same irradiation time (36 h) in the absence of contaminants. Following immersion of the photocatalyst in water with a pH of 6 and 8.5 for 36 h in the absence of light, the concentration of Cu in solution was found to be less than 15 ppb and 8 ppb, for pollen-Cu@ Cu_2O @CuO and pollen-Cu@ Cu_2O @CuO@CuS, respectively. This suggests that the photocorrosion is primarily attributable to the hole-electron pairs, as the hybrids display robust chemical stability under these conditions.

To illustrate the potential of hybrid photocatalysts in the degradation and mineralization of organic compounds, we conducted a study on the mineralization of a multipollutant solution. Specifically, we investigated the photocatalytic degradation and mineralization of a pharmaceutical mixture containing lansoprazole, levofloxacin, and TC (60 ppm) using TOC measurements after a period of 4 h. This study offers preliminary insight into the performance of the photocatalyst in a complex, multicomponent matrix. As with previous experiments, superior performance was observed under pH 8.5 conditions (Figure 3g). The high rate of mineralization indicated that the photocatalyst has significant potential for the degradation and mineralization of organic contaminants. In light of these findings, it can be concluded that onion-like pollen-Cu@ Cu_2O @CuO@CuS photocatalysts are highly efficacious in the degradation and mineralization of persistent and emerging organic pollutants at concentrations that are challenging to remove through conventional processes, particularly in comparison to the current state of the art in the search for new photocatalysts.

2.3. Recyclability of Onion-Like Pollen-Cu@ Cu_2O @CuO@CuS Hybrid Photocatalysts

Once the useful life of the photocatalyst has come to an end, its recyclability for the production of pollen pellets (i.e., non-woody biofuels) is evaluated. This approach is based on the principles of chemistry and the green and circular economy, with the aim of minimizing waste production and enhancing the efficient utilization of natural resources. In accordance with the ISO 17225–6:2014 standard for non-wood pellets, these pellets may be deemed commercial biofuels if they meet specific criteria: ash

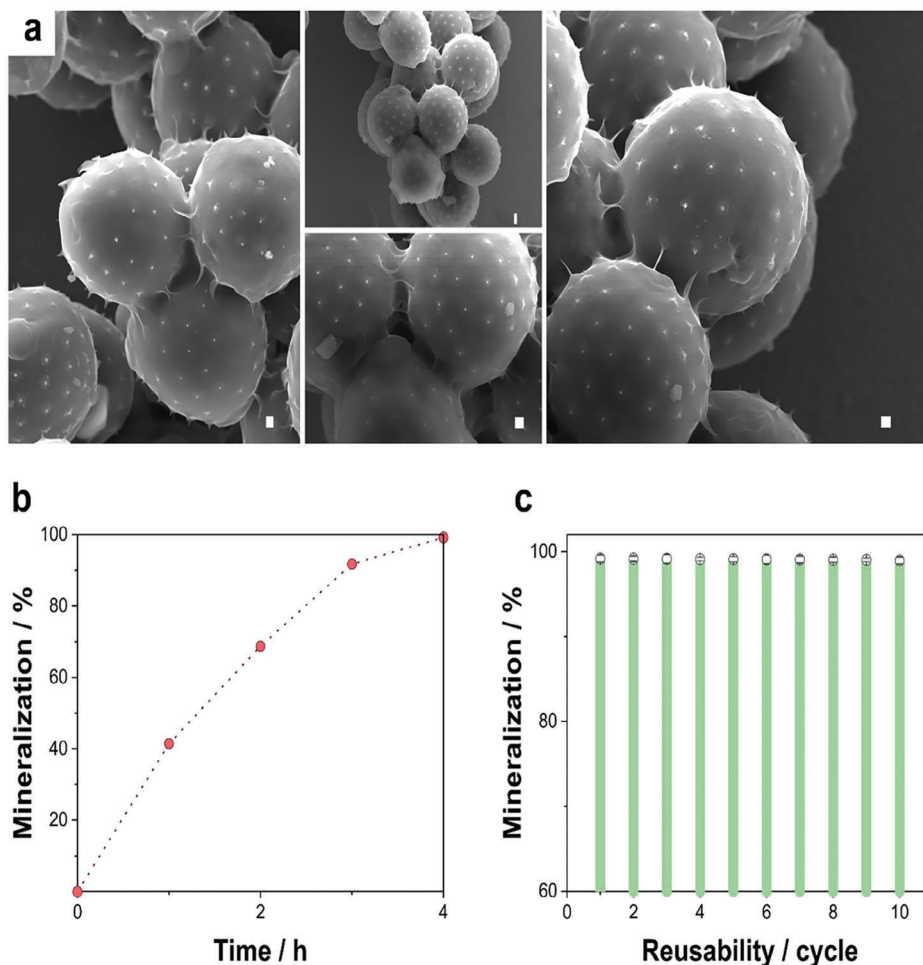


Figure 4. a) FE-SEM micrographs of pollen ashes. Scale bar: 1 μm . b) Mineralization performance of a multipollutant solution containing 20 ppm each of lansoprazole, levofloxacin, and tetracycline (total 60 ppm) during a 4-h period under visible light irradiation at pH 7.0 using pollen ashes and PMS. c) Reusability performance of pollen ashes in mineralizing a multipollutant solution containing 20 ppm each of lansoprazole, levofloxacin, and tetracycline during a 4-h period under visible light irradiation at pH 7.0 and PMS. The error bars represent the standard deviations from 3 replicate experiments. Experimental conditions: [pollutants] = 60 ppm (tetracycline, levofloxacin, and lansoprazole), [PMS] = 0.85 mM, catalyst dosage = 1 mg mL⁻¹.

content less than 10% by weight, moisture content less than 15% by weight, and a calorific value greater than 14.5 MJ kg⁻¹.

In the case of pollen pellets derived from the photocatalysts, the exhibit an ash content was less than 7% by weight, the moisture content was less than 8%, and the calorific value was $\approx 22.1 \pm 0.3$ MJ kg⁻¹. It is noteworthy that the ash residue resulting from the combustion of the pellets constitutes only 7% by weight of the original mass of the photocatalyst. As complementary use, the ash residue was employed for the activation of PMS, which was utilized for the mineralization of a multicomponent solution containing lansoprazole, levofloxacin, and tetracycline, each at a concentration of 20 ppm and a pH of 7.0.

The analysis of pollen ash morphology revealed the presence of spherical, regular microparticles with a diameter of $\approx 10\text{--}14$ μm in size (Figure 4a). Furthermore, these particles formed various aggregates, such as rods and geometric sheets, which resulted in openings and high porosity. Although the spikes no longer maintained the original pollen architecture, they were still faintly discernible, albeit notably shorter in length. These characteristics

facilitated the activation of PMS and subsequent mineralization of organic pollutants in wastewater.

Figure 4b illustrates the mineralization rate of the 60-ppm drug solution after 4 h in the dark and under visible light. In both instances, the mineralization rate exceeded 99%. However, when the sample was irradiated with visible light, the mineralization values exhibited a slight increase at shorter times. Figure 4c depicts the mineralization rates over the course of 10 successive cycles, each comprising 4 h, which were exclusively conducted under visible light irradiation. The data demonstrate that the rate of mineralization remains constant throughout the 10 cycles, indicating that these materials are effective PMS activators. It is crucial to highlight that the ashes were not subjected to any form of treatment throughout the entire reuse process.

3. Conclusion

To address the issue of contamination of water sources by emerging and persistent organic pollutants, innovative water treatment

methods have been developed. Recent research has employed pollen as a precursor to synthesize highly efficient onion-like pollen-Cu@Cu₂O@CuO@CuS photocatalysts, leveraging the principles of green and circular chemistry. The photocatalysts demonstrate remarkable efficacy in the degradation and mineralization of organic pollutants. The study proposes a circular process whereby the used photocatalysts are recycled to produce biopellets for waste-to-energy conversion. The resulting ashes are repurposed as PMS activators for the mineralization of pharmaceuticals from wastewater, thereby reducing the generation of waste.

The synthesis process employs a sequential and scalable electrochemical production method that preserves the structural integrity and size uniformity of sunflower pollen. The resulting photocatalyst exhibits a markedly elevated surface area, which can be attributed to its intricate multilayered structure and irregular surface topography. This enhances the photocatalyst's capacity for light harvesting and pollutant adsorption. The successful deposition of copper, Cu₂O, CuO, and CuS layers, forming an onion-like architecture, is confirmed by the application of characterization techniques. These hybrids demonstrate the suppression of electron-hole recombination and exhibit broad absorption in the visible light and near-infrared regions, indicating their potential for visible-light-driven photocatalytic water decontamination.

The study evaluates the efficacy of the photocatalyst in degrading and mineralizing the antibiotic TC under different pH conditions. The results show rapid degradation and over 99% mineralization achieved after 90 min of visible light irradiation. The photocatalyst is resistant to photocorrosion and has low Cu ion release, highlighting its stability and versatility under varying environmental conditions. The study examines the effectiveness of the photocatalyst in degrading a pharmaceutical multipollutant solution, making it a promising candidate for water purification applications. Additionally, the study demonstrates the recycling of used photocatalysts into pollen biopellets, which meet the criteria for commercial biofuels with low ash and moisture content and high calorific value (ash content <7% by weight, moisture content <8% by weight, and a calorific value of $\approx 22.1 \pm 0.3$ MJ kg⁻¹). The ash residue resulting from this process has been demonstrated useful as an effective PMS activator for mineralizing organic pollutants in wastewater. It achieves over 99% mineralization rates even under dark conditions. The ash demonstrates consistent mineralization rates over ten consecutive cycles, indicating its robustness as a reusable PMS activator without requiring additional treatment.

This research presents a holistic approach to water treatment and waste management. It offers practical solutions for pollutant removal while minimizing waste production. The study contributes to sustainable resource utilization and environmental remediation efforts by integrating green and circular chemistry principles.

4. Experimental Section

Electrosynthesis and Characterization of Pollen-Cu@Cu₂O@CuO@CuS Photocatalyst: Pollen from *Helianthus Annuus*, sourced from BONAPOL, A.S. in the Czech Republic in 2019, was used as the biotemplate for photocatalyst synthesis. The process involved immersing 100 mg of pollen in glacial acetic acid for 15 min, followed by thorough

washing with MilliQ water. The treated pollen was then introduced into a stannous palladization bath, which was prepared by slowly adding 0.2 g of SnCl₂ to a 50 mL solution of PdCl₂ (0.5 mM) and HCl (0.2 M). After the complete dissolution of SnCl₂, an additional 1.6 g of SnCl₂ was added to prevent hydrolysis and the formation of insoluble Sn(OH)Cl. The pollen was then immersed in the bath at 500 rpm and 35 °C for 35 min. Afterward, it was filtered and washed with HCl (1 M), PBS, and MilliQ water. For the next step, a solution containing CuSO₄ (0.04 M), potassium bitartrate (0.05 M), EDTA (0.07 M), formaldehyde (1 M), NaOH (0.25 M), and thiourea (1.3 μM) at pH 12 with NaOH was prepared. The palladized pollen was then added to the solution and stirred at room temperature (25 °C) for 120 min. Afterward, it was filtered washed with MilliQ water. The pollen was subjected to oxidation at 200 °C for 8 h, followed by sulphidation through immersion in 50 mL of thioacetamide (30 mM) at 85 °C for 4 h.^[40,59,60] The resulting photocatalyst was filtered and washed with MilliQ water.

The surface morphology and architecture of photocatalysts based on pollen were examined using field emission scanning electron microscopy (FE-SEM; JEDL J-7100) equipped with an energy-dispersive X-ray spectroscopy (EDX) detector. The elemental composition was determined using EDX equipment. The thermal stability of pollen and hybrid photocatalysts was evaluated through thermogravimetric analysis (TGA) with a Mettler TGA/SDTA851e (Mettler Toledo AG) analyzer. The analysis was conducted at a heating rate of 10 °C min⁻¹ from room temperature to 800 °C in an air atmosphere. The crystalline phase of hybrid photocatalysts was determined using Bruker D8 Venture X-ray single crystal diffractometer with Cu Kα1 radiation ($\lambda = 1.5406$ Å), operating at 45 kV and 40 mA. The photocatalyst's specific surface area was determined using the Brunauer-Emmett-Teller (BET) method, which was based on N₂ adsorption-desorption isotherms measured at 77 K. The Micromeritics Tristar-II was used for this purpose. To analyze the surface chemical composition, X-ray photoelectron spectrometry (XPS) was used. The samples were irradiated with monochromated X-rays from an Al Kα source with a spot size of 200 μm in an ultra-high vacuum. Ejected electrons were collected at a 45-degree emission angle and directed toward a hemispherical capacitor analyzer in fixed-analyzer-transmission mode. The measurements were conducted using an active low-voltage ion gun and electron neutralizer. Spectrometer calibration was performed following ISO 15 472:2010, utilizing etched clean surfaces of pure copper, silver, and gold to ensure an accuracy of less than 0.2 eV. Survey spectra were obtained using a pass energy of 280 eV and a step size of 1 eV. High-resolution spectra were collected with a pass energy of 55 eV and a finer step size of 0.05 eV. The photocatalyst's optoelectronic properties were analyzed using a UV-Vis spectrophotometer (PerkinElmer, Lambda 900 UV) and UV-Vis diffuse reflectance spectra (DRS).

Pollutant Degradation Experiments: This study employed a UV-Vis spectrophotometer (UV-1800 Shimadzu) and high-performance liquid chromatography mass-spectroscopy (HPLC-MS, Waters Xevo G2-XS QToF system) to measure tetracycline (TC) concentrations under various reaction times and irradiation conditions. The mobile phase was a 0.1% (v/v) aqueous solution of formic acid, which facilitated elution at a flow rate of 0.2 mL min⁻¹. A linear gradient was used, transitioning from 90% aqueous solution of formic acid and 10% acetonitrile to a final composition of 10% aqueous solution of formic acid and 90% acetonitrile over a period of 4 min. Mass spectrometry analysis was performed using an electrospray ionization source in positive ion mode. Total organic content (TOC) in the aqueous solution was measured using TOC-VCSH (Shimadzu) to assess mineralization. Photocatalytic experiments were conducted using a 1.6 W white LED strip (2.2×10^{-3} W cm⁻²) and solar light.

The effectiveness of the photocatalyst was evaluated by examining TC persistence under non-photolytic or photocatalytic conditions. Two TC 20 ppm solutions with pH values of 6.0 and 8.5 were stored in the dark at room temperature for 30 days. To monitor the degradation of TC, daily UV-Vis spectrum readings and TOC determinations were conducted. The photolytic stability of 25 mL of TC 20 ppm at pH 6.0 and 8.5 was assessed by irradiating it for 3 h with an LED, accompanied by periodic UV-Vis spectrum readings and TOC measurements.

The adsorption-desorption equilibrium time was determined by adding 10 mg of photocatalyst to two 25 mL solutions of TC 20 ppm at pH 6.0 and 8.5. The solutions were stored in the dark under constant stirring for 3 h, with periodic UV–Vis spectrum readings.

Photocatalytic degradation and mineralization of TC were analyzed by adding 10 mg of the photocatalyst to two 25 mL TC 20 ppm solutions at pH 6.0 and 8.5. After storing in the dark for 90 min to ensure complete antibiotic adsorption, the LED was turned on, and the mixture was irradiated for 3 h. Periodic UV–Vis spectrum readings and TOC measurements were taken. The study also assessed the influence of inorganic anions on photocatalytic efficiency by examining the degradation and mineralization of a 20 ppm TC solution in the presence of 10 and 100 mM concentrations of chlorides, nitrates, and phosphates individually. UV–Vis lectures were conducted at 0, 30, 60, and 90 min, and 1 mL samples were stored for TOC analysis at 0, 60, and 90 min. The experiments were triplicated and conducted at pH 6.0 and 8.5. To determine the role of different reactive oxygen species during photocatalysis, 1 mM of various quenchers was added independently to a 20 ppm TC solution. The quenchers used were isopropyl alcohol (quencher of hydroxyl radicals), benzoquinone (quencher of superoxide radicals), and triethanolamine (quencher of valence band holes). TC concentrations were determined using HPLC-MS. To evaluate the efficiency decay and reusability of the photocatalyst, the degradation, and mineralization of TC were repeated 24 times for each pH using the same photocatalyst sample. During photocatalysis, 1 mL of the TC solution was sampled at 0, 60, and 90 min for TOC analysis. This experiment was triplicated. Finally, the photocatalyst performance was tested in the degradation and mineralization of a mixture solution of lansoprazole, levofloxacin, and tetracycline, each at a concentration of 20 ppm. 50 mL of the solution at pH 6.0 and 8.5 was irradiated for 4 h after adding 40 mg of photocatalyst. The TOC was measured at 1-h intervals.

Recyclability of Pollen-Cu@Cu₂O@CuO@CuS Photocatalyst: The research was conducted on pollen-based photocatalysts to produce environmentally friendly non-wood biopellets through a cylindrical pelletization process using a single mechanical pelletizer. The process involved several steps, including harvesting, pretreatment, pelletization, and post-treatment. The pollen structures were dried at 30 °C to achieve a humidity level of ≈10%–15% (w/w). The pelletizer cylinder was preheated to 55 °C before introducing the pollen biomass. The cylinder was then loaded with pollen biomass until full and compressed at a maximum force of 3500 N for 90 s. The resulting pellet was removed from the cylinder by moving the crosshead downward and cooled to room temperature. In accordance with the UNE-EN ISO 18134-2 standard, we assessed the humidity content of pollen pellets using a balance with an accuracy of ±0.0001 g and an oven heated to 105 °C. We determined the calorific power using an IKA calorimeter C 5000.

To obtain pollen pellet ashes, we combusted them in a Heraeus M110 Muffel oven at 1000 °C. The pollen ashes were characterized morphologically using a field emission scanning electron microscope (FE-SEM, Hitachi S-4800) equipped with an energy-dispersive X-ray spectroscopy detector. The resulting ashes from the combustion process were used as catalysts and photocatalysts to activate peroxymonosulphate (PMS) for the mineralization of a multicomponent solution containing Lansoprazole, Levofloxacin, and Tetracycline, each at a concentration of 20 ppm and pH 7.0. The total organic carbon (TOC) was measured at 1-h intervals during 4 h. The reusability of the ashes was demonstrated by using them for 10 successive cycles.

Statistical Analysis: Prior to analysis, the data underwent pre-processing through normalization to ensure consistency and comparability across different experimental runs. Outliers were identified and removed using the Grubbs test, with a significance level of 0.05. To ensure the reproducibility and reliability of the results, each statistical analysis was performed in triplicate ($n = 3$).

Supporting Information

Supporting Information is available from the Wiley Online Library or from the author.

Acknowledgements

Grant Project PID2020-115663GB-C32 financed by MICIU/ AEI / 10.13039/501100011033. The authors thank the CCI-UB for the use of their equipment.

Conflict of Interest

The authors declare no conflict of interest.

Data Availability Statement

The data that support the findings of this study are available from the corresponding author upon reasonable request.

Keywords

biohybrid photocatalysts, biomimetic photocatalysts, circular chemistry, peroxymonosulphate activation, photocatalytic water treatment

Received: June 25, 2024

Revised: July 26, 2024

Published online:

- [1] Y. Pi, X. Li, Q. Xia, J. Wu, Y. Li, J. Xiao, Z. Li, *Chem. Eng. J.* **2018**, *337*, 351.
- [2] K. Breivik, J. M. Armitage, F. Wania, A. J. Sweetman, K. C. Jones, *Environ. Sci. Technol.* **2016**, *50*, 798.
- [3] F. C. Moreira, R. A. R. Boaventura, E. Brillas, V. J. P. Vilar, *Appl. Catal. B Environ.* **2017**, *202*, 217.
- [4] M. A. Ashraf, *Environ. Sci. Pollut. Res.* **2017**, *24*, 4223.
- [5] S. Zhang, B. Li, X. Wang, G. Zhao, B. Hu, Z. Lu, T. Wen, J. Chen, X. Wang, *Chem. Eng. J.* **2020**, *390*, 124642.
- [6] A. Serrà, L. Philippe, F. Perreault, S. Garcia-Segura, *Water Res.* **2021**, *188*, 116543.
- [7] O. M. L. Alharbi, A. A. Basheer, R. A. Khattab, I. Ali, *J. Mol. Liq.* **2018**, *263*, 442.
- [8] M. Barletta, A. R. A. Lima, M. F. Costa, *Sci. Total Environ.* **2019**, *651*, 1199.
- [9] A. J. Jamieson, T. Malkocs, S. B. Piertney, T. Fujii, Z. Zhang, *Nat. Ecol. Evol.* **2017**, *1*, 24.
- [10] X. Ren, G. Zeng, L. Tang, J. Wang, J. Wan, Y. Liu, J. Yu, H. Yi, S. Ye, R. Deng, *Sci. Total Environ.* **2018**, *610–611*, 1154.
- [11] A. Serrà, E. Gómez, N. al Hoda al Bast, Y. Zhang, M. Duque, M. José Esplandiú, J. Esteve, J. Nogués, B. Sepúlveda, *Chem. Eng. J.* **2024**, *487*.
- [12] Z. Zhang, J. Liang, W. Zhang, M. Zhou, X. Zhu, Z. Liu, Y. Li, Z. Guan, C. S. Lee, P. K. Wong, H. Li, Z. Jiang, *Appl. Catal. B Environ.* **2023**, *330*, 122621.
- [13] A. Rafiq, M. Ikram, S. Ali, F. Niaz, M. Khan, Q. Khan, M. Maqbool, *J. Ind. Eng. Chem.* **2021**, *97*, 111.
- [14] D. Wang, M. A. Mueses, J. A. C. Márquez, F. Machuca-Martínez, I. Grčić, R. Peralta Muniz Moreira, G. L. Puma, *Water Res.* **2021**, *202*, 117421.
- [15] E. Gómez, R. Cestaro, L. Philippe, A. Serrà, *Appl. Catal. B Environ.* **2022**, *317*.
- [16] L. Xu, Y. Liu, L. Li, Z. Hu, J. C. Yu, *ACS Catal.* **2021**, *11*, 14480.
- [17] B. Wang, Z. Jiang, J. C. Yu, *J. Mater. Chem. A* **2019**, *7*, 9335.
- [18] Y. Lu, H. Zhang, D. Fan, Z. Chen, X. Yang, *J. Hazard. Mater.* **2022**, *423*, 127128.
- [19] A. Serrà, E. Gómez, J. Michler, L. Philippe, *Chem. Eng. J.* **2021**, *413*, 127477.

- [20] S. Mosleh, M. R. Rahimi, M. Ghaedi, K. Dashtian, S. Hajati, *Ultrason. Sonochem.* **2018**, *40*, 601.
- [21] J. Singh, S. Juneja, R. K. Soni, J. Bhattacharya, *J. Colloid Interface Sci.* **2021**, *590*, 60.
- [22] Y. T. Kao, S. M. Yang, K. C. Lu, *Materials* **2019**, *12*, 1106.
- [23] W. Zhu, Q. Yang, J. Du, P. Yin, J. Yi, Y. Liu, X. Wu, Z. Zhang, *Curr. Appl. Phys.* **2022**, *39*, 113.
- [24] L. Isac, C. Cazan, A. Enesca, L. Andronic, *Front. Chem.* **2019**, *7*, 1.
- [25] E. Brillas, A. Serrà, S. Garcia-Segura, *Curr. Opin. Electrochem.* **2021**, *26*, 100660.
- [26] X. Liu, Z. Guo, L. Zhou, J. Yang, H. Cao, M. Xiong, Y. Xie, G. Jia, *Chemosphere* **2019**, *222*, 38.
- [27] X. Lu, Z. Li, Y. Liu, B. Tang, Y. Zhu, J. M. Razal, E. Pakdel, J. Wang, X. Wang, *J. Clean. Prod.* **2020**, *246*, 118949.
- [28] K. An, D. Yang, X. Zhao, H. Ren, Z. Zhao, Y. Chen, Z. Zhou, W. Wang, Z. Jiang, *Mater. Chem. Phys.* **2020**, *256*, 123621.
- [29] A. Serrà, P. Pip, E. Gómez, L. Philippe, *Appl. Catal. B Environ.* **2020**, *268*, 118745.
- [30] A. Serrà, Y. Zhang, B. Sepúlveda, E. Gómez, J. Nogués, J. Michler, L. Philippe, *Water Res.* **2020**, *169*, 115210.
- [31] A. Serrà, R. Artal, J. García-Amorós, B. Sepúlveda, E. Gómez, J. Nogués, L. Philippe, *Adv. Sci.* **2020**, *7*, 1902447.
- [32] K. Xiao, T. Wang, M. Sun, A. Hanif, Q. Gu, B. Tian, Z. Jiang, B. Wang, H. Sun, J. Shang, P. K. Wong, *Environ. Sci. Technol.* **2020**, *54*, 537.
- [33] G. Tzvetkov, N. Kaneva, T. Spassov, *Appl. Surf. Sci.* **2017**, *400*, 481.
- [34] H. Hamrouni, I. Jaouali, M. F. Nsib, E. Fazio, F. Neri, A. Bonavita, S. G. Leonardi, G. Neri, *J. Mater. Sci. Mater. Electron.* **2018**, *29*, 11096.
- [35] F. Cao, D. X. Li, *Biomed. Mater.* **2009**, *4*, 025009.
- [36] S. R. Hall, V. M. Swinerd, F. N. Newby, A. M. Collins, S. Mann, *Chem. Mater.* **2006**, *18*, 598.
- [37] K. Tian, X. X. Wang, H. Y. Li, R. Nadimicherla, X. Guo, *Sensors Actuators, B Chem* **2016**, *227*, 554.
- [38] S. Azizi, F. Namvar, R. Mohamad, P. Md Tahir, M. Mahdavi, *Mater. Lett.* **2015**, *148*, 106.
- [39] Y. Liu, X. Zhang, B. Wu, H. Zhao, W. Zhang, C. Shan, J. Yang, Q. Liu, *ChemistrySelect* **2019**, *4*, 12445.
- [40] H. Li, Z. Su, S. Hu, Y. Yan, *Appl. Catal. B Environ.* **2017**, *207*, 134.
- [41] F. Zhang, S. Huang, Q. Guo, H. Zhang, H. Li, Y. Wang, J. Fu, X. Wu, L. Xu, M. Wang, *Colloids Surfaces A Physicochem. Eng. Asp.* **2020**, *602*, 125076.
- [42] D. Ranjith Kumar, D. Manoj, J. Santhanalakshmi, *Sensors Actuators, B Chem* **2013**, *188*, 603.
- [43] X. Chang, J. Liu, Z. Guo, Y. Cheng, Q. Yan, Y. Y. Li, *Appl. Catal. B Environ.* **2024**, *349*, 123858.
- [44] Y. Wang, X. Li, W. Xu, D. Chen, N. Li, Q. Xu, H. Li, J. Lu, *Appl. Catal. B Environ.* **2024**, *348*, 123839.
- [45] S. Li, C. Wang, Y. Liu, M. Cai, Y. Wang, H. Zhang, Y. Guo, W. Zhao, Z. Wang, X. Chen, *Chem. Eng. J.* **2022**, *429*, 132519.
- [46] S. Li, C. Wang, Y. Liu, B. Xue, W. Jiang, Y. Liu, L. Mo, X. Chen, *Chem. Eng. J.* **2021**, *415*, 128991.
- [47] H. T. Ren, W. B. Cao, J. Qin, C. C. Cai, D. S. Li, T. T. Li, C. W. Lou, J. H. Lin, *Sep. Purif. Technol.* **2024**, *341*, 126910.
- [48] R. C. Pawar, C. S. Lee, *Nanomater.-Based Photocat.* **2015**, *25*.
- [49] M. Krivec, R. Dillert, D. W. Bahnemann, A. Mehle, J. Štrancar, G. Dražič, *Phys. Chem. Chem. Phys.* **2014**, *16*, 14867.
- [50] M. Delarmelina, M. W. Dlamini, S. Pattison, P. R. Davies, G. J. Hutchings, C. R. A. Catlow, *Phys. Chem. Chem. Phys.* **2023**, *25*, 4161.
- [51] F. Zaviska, P. Drogui, E. M. El Hachemi, E. Naffrechoux, *Ultrason. Sonochem.* **2014**, *21*, 69.
- [52] X. Gao, Q. Guo, G. Tang, W. Peng, Y. Luo, D. He, *J. Water Reuse Desalination* **2019**, *9*, 301.
- [53] T. Tang, G. Lu, W. Wang, R. Wang, K. Huang, Z. Qiu, X. Tao, Z. Dang, *Chemosphere* **2018**, *206*, 26.
- [54] A. G. Rincón, C. Pulgarin, *Appl. Catal. B Environ.* **2004**, *51*, 283.
- [55] C. Hu, J. C. Yu, Z. Hao, P. K. Wong, *Appl. Catal. B Environ.* **2003**, *46*, 35.
- [56] O. Yepsen, J. Yáñez, H. D. Mansilla, *Sol. Energy* **2018**, *171*, 106.
- [57] H. Xing, E. Lei, Z. Guo, D. Zhao, X. Li, Z. Liu, *Inorg. Chem. Front.* **2019**, *6*, 2488.
- [58] C. Y. Toe, Z. Zheng, H. Wu, J. Scott, R. Amal, Y. H. Ng, *Angew. Chem., Int. Ed.* **2018**, *57*, 13613.
- [59] X. Jiang, T. Herricks, Y. Xia, *Nano Lett.* **2002**, *2*, 1333.
- [60] M. Kaur, K. P. Muthe, S. K. Deshpande, S. Choudhury, J. B. Singh, N. Verma, S. K. Gupta, J. V. Yakhmi, *J. Cryst. Growth* **2006**, *289*, 670.